

## Supporting Information

### Reassessing Anionic Redox in Conventional Layered Oxide Cathodes for Li-Ion Batteries: Ionic and Covalent Mechanisms

Authors: Jianhua Yin,<sup>a</sup> Zixin Wu,<sup>a\*</sup> Kai Fang,<sup>a</sup> Yuanlong Zhu,<sup>a</sup> Kang Zhang,<sup>a</sup> Haitang Zhang,<sup>a</sup> Yilong Chen,<sup>a</sup> Li Li,<sup>a</sup> Longlong Fan,<sup>b</sup> Kang Dong,<sup>b</sup> Lirong Zheng,<sup>b</sup> Qingsong Wang,<sup>c\*</sup> Huan Huang,<sup>b\*</sup> Jing Zhang,<sup>b\*</sup> Yu Qiao <sup>a\*</sup> and Shi-Gang Sun <sup>a</sup>

#### Affiliations:

<sup>a</sup> State Key Laboratory of Physical Chemistry of Solid Surfaces, iChEM (Collaborative Innovation Center of Chemistry for Energy Materials), Department of Chemistry, College of Chemistry and Chemical Engineering, Xiamen University, Xiamen, 361005, P.R. China

<sup>b</sup> Beijing Synchrotron Radiation Facility, Institute of High Energy Physics, Chinese Academy of Sciences, Beijing, 100049, P. R. China

<sup>c</sup> Bavarian Center for Battery Technology (BayBatt), Department of Chemistry, University of Bayreuth, Universitätsstrasse 30, Bayreuth 95447, Germany

\* Correspondence to:

[zixinwu\\_gz@163.com](mailto:zixinwu_gz@163.com) (Z. W.);

[qingsong.wang@uni-bayreuth.de](mailto:qingsong.wang@uni-bayreuth.de) (Q. W.);

[huanhuang@ihep.ac.cn](mailto:huanhuang@ihep.ac.cn) (H. H.);

[jzhang@ihep.ac.cn](mailto:jzhang@ihep.ac.cn) (J. Z.);

[yuqiao@xmu.edu.cn](mailto:yuqiao@xmu.edu.cn) (Y. Q.)

## Methods / Experimental Procedures

### Electrolytes and Electrode Preparation

The electrolyte consisted of 1 M LiPF<sub>6</sub> in a solvent mixture of 30% wt ethylene carbonate (EC) and 70% wt ethyl methyl carbonate (EMC), supplied by DoDoChem. The slurry comprised LiNi<sub>1/3</sub>Co<sub>1/3</sub>Mn<sub>1/3</sub>O<sub>2</sub> (NCM333, Contemporary Amperex Technology Co. Ltd) active material, carbon black (Super-P, Canrd) and polyvinylidene fluoride (PVDF, Canrd, 5%wt) (90:5:5, by weight ratio). The slurry (N-methyl pyrrolidone (NMP, Canrd) as dissolving solvent for the PVDF binder) was homogeneously coated onto a carbon-coated aluminum foil (Suzhou Siner Technology Co., Ltd.) current collector and dried at 110 °C for 12 h in a vacuum oven. The electrodes for LiNi<sub>0.8</sub>Co<sub>0.1</sub>Mn<sub>0.1</sub>O<sub>2</sub> (NCM811, Contemporary Amperex Technology Co. Ltd) were prepared using the same procedure. The loading mass of the active materials for both NCM333 and NCM811 electrodes was approximately 5 to 8 mg/cm<sup>2</sup>.

### Cell Assembly

The NCM333 and NCM811 electrodes were respectively assembled into 2032 coin cells (Shenzhen TeenSky Technology Co., Ltd.). Each half-cell was constructed by successively stacking a lithium metal foil negative electrode (thickness, 0.5 mm), a Celgard-2325 separator, and either an NCM333 or NCM811 cathode, with 75 μL of electrolyte added. Assembly took place in an argon-filled glove box with moisture and oxygen levels maintained below 0.01 ppm.

### Electrochemical Measurements

For the coin cell, galvanostatic electrochemical measurements were conducted under potential control using the Neware Battery Test System (CT-4008T-5V10mA-164, Shenzhen, China) at a constant temperature of 26 °C. The galvanostatic charge tests were performed at 0.5 C within a voltage range of 3.0-4.2/4.5/4.8 V (where 1 C = 100 mA/g).

## Characterizations

### X-ray absorption fine structure (XAFS)

XAFS measurements at the Ni (8333 eV), Co (7709 eV), and Mn (6539 eV) K-edge were conducted in transmission mode at the 1W1B station of the Beijing Synchrotron Radiation Facility (BSRF, P. R. China) using a double crystal Si (111) monochromator detuned to 60~70 % of its original intensity to eliminate the high order harmonics. The BSRF storage rings at BSRF operated at 2.5 GeV with a maximum current of 250 mA. Ni, Co, and Mn foils were detected in the transmission mode to serve as the reference for energy calibration. The XAFS data were processed and analyzed using the Demeter software package<sup>1</sup>. A linear function was subtracted from the pre-edge region, while the background contribution above the post-edge region was fitted to a fourth-order polynomial (cubic spline). Then, the edge jump was normalized using Athena software<sup>1</sup>. The normalized  $k^3$ -weighted EXAFS spectra were Fourier transformed in  $k$  space with integration limits of 3.15 - 13.2  $\text{\AA}^{-1}$  for the Ni data, 3.0 - 11.1  $\text{\AA}^{-1}$  for the Co data, and 3.15 - 10.1  $\text{\AA}^{-1}$  for the Mn data using a Hanning window ( $dk = 1.0 \text{\AA}^{-1}$ ). EXAFS structural parameters were obtained by nonlinear least-squares analysis of the data using amplitude and phase functions generated from the FEFF6 code<sup>2, 3</sup>. The value of amplitude reduction factor  $S_0^2$  was scaled to a fixed value of 0.85 for the Ni edge, 0.80 for the Co edge, and 0.75 for the Mn edge, respectively, after the refinements of the pristine state.

### Near-edge X-ray absorption fine structure (NEXAFS)

NEXAFS measurements at the Ni, Co, and Mn  $L_{2,3}$ -edge were performed in total electron yield (TEY) mode at the 4B9B station of the Beijing Synchrotron Radiation Facility (BSRF, P.R. China). The BSRF storage rings at BSRF operated at 2.5 GeV with a maximum current of 250 mA. Samples were attached to a copper specimen holder using conductive carbon tape within an argon-filled glove box, transferred to a container, and then into an X-ray absorption antechamber, all maintained within an argon environment to minimize the potential exposure to air. Data were collected with a spectral resolution of approximately 0.1 eV. The energy scale for all  $L_{2,3}$ -edge spectra was calibrated using the gold (Au)  $4f_{7/2}$  binding energy at 84 eV. The simulation of Ni  $L_{2,3}$ -edge using CTM4XAS<sup>4</sup>. During the simulation process, the ligand field energy is set to 1 eV, 2 eV, 3 eV, and 4 eV, respectively, while the ligand-to-metal charge transfer energy varies from -15 eV to 15 eV in 1 eV increments. The core hole potential  $U_{pd}$  and the on-site Coulomb interactions  $U_{dd}$  were kept constant ( $U_{pd} - U_{dd} = 1 \text{ eV}$ ).

## **Resonant inelastic X-ray scattering (RIXS)**

The RIXS experiments in this study were conducted at the U41-PEAXIS beamline of the BESSY II synchrotron at Helmholtz-Zentrum Berlin (HZB, Berlin, Germany)<sup>5</sup>. Electrodes at specific states of charge were removed from the coin cells, rinsed with dimethyl carbonate (DMC), and dried under vacuum. The electrode samples were then mounted on the sample holder using adhesive copper tape. RIXS spectra were collected at an excitation energy of 531 eV, with adhesive carbon tape used for energy calibration. The structural illustrations of TM migration and trapped-O<sub>2</sub> were created using the VESTA visualization program<sup>6</sup>.

## Supplementary Figures/Tables

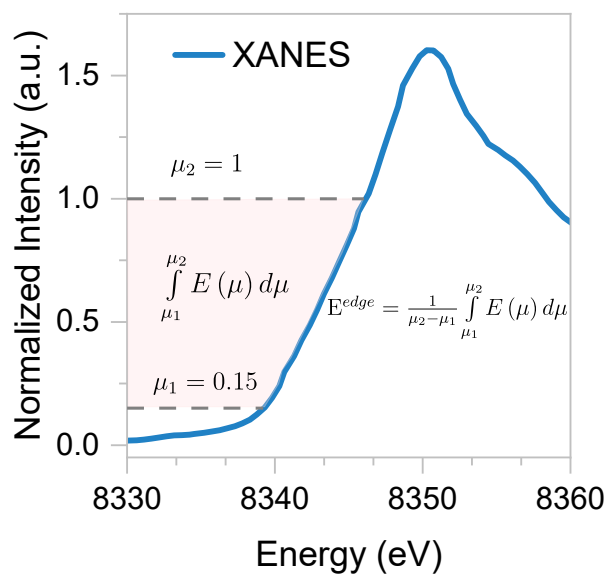


**Figure S1. Details of Determining the  $E_0$  of K-edge XANES.** The integral method<sup>7</sup> is used for determining the oxidation states of transition metals from their K-edge XANES spectra.

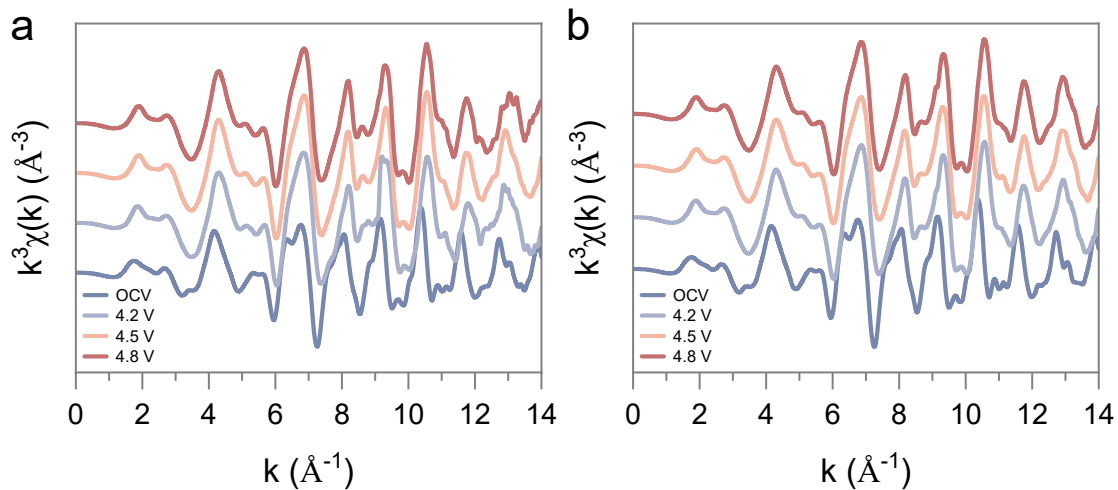


**Figure S2.  $k^3$ -weighted EXAFS oscillations at the Ni K-edge.** (a) Ni K-edge EXAFS spectra of  $\text{LiNi}_{1/3}\text{Co}_{1/3}\text{Mn}_{1/3}\text{O}_2$  (NCM333) at the pristine state and various charge states. (b) Ni K-edge EXAFS spectra of  $\text{LiNi}_{0.8}\text{Co}_{0.1}\text{Mn}_{0.1}\text{O}_2$  (NCM811) at the pristine state and various charge states. The distinct frequencies in  $\chi(k)$  correspond to different near-neighbor coordination shells. The smooth oscillation curves demonstrate high data quality, with the signal-to-noise ratio ensuring the credibility of subsequent analysis.

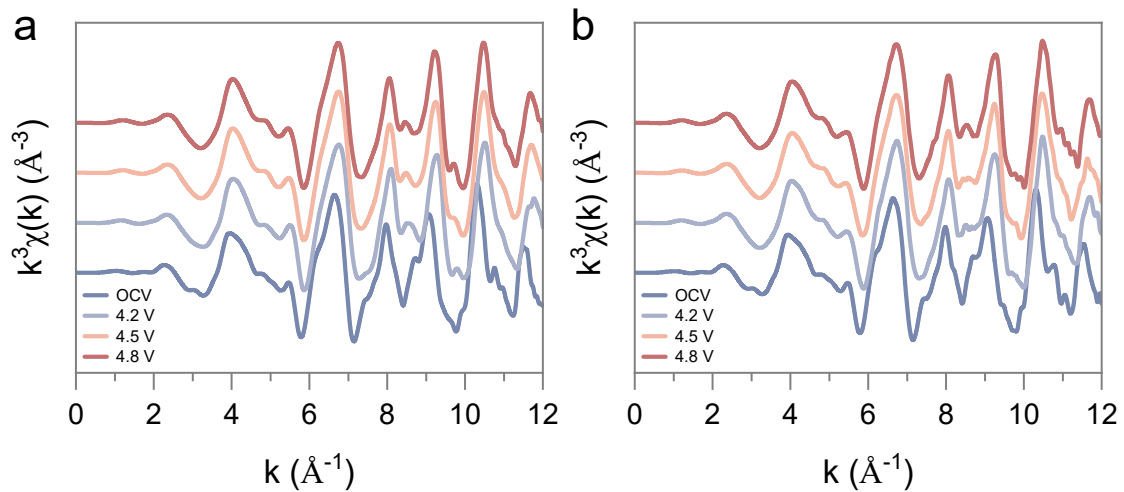


**Figure S3.  $k^3$ -weighted EXAFS oscillations at the Co K-edge.** (a) Co K-edge EXAFS spectra of  $\text{LiNi}_{1/3}\text{Co}_{1/3}\text{Mn}_{1/3}\text{O}_2$  (NCM333) at the pristine state and various charge states. (b) Co K-edge EXAFS spectra of  $\text{LiNi}_{0.8}\text{Co}_{0.1}\text{Mn}_{0.1}\text{O}_2$  (NCM811) at the pristine state and various charge states. The distinct frequencies in  $\chi(k)$  correspond to different near-neighbor coordination shells. The smooth oscillation curves demonstrate high data quality, with the signal-to-noise ratio ensuring the credibility of subsequent analysis.

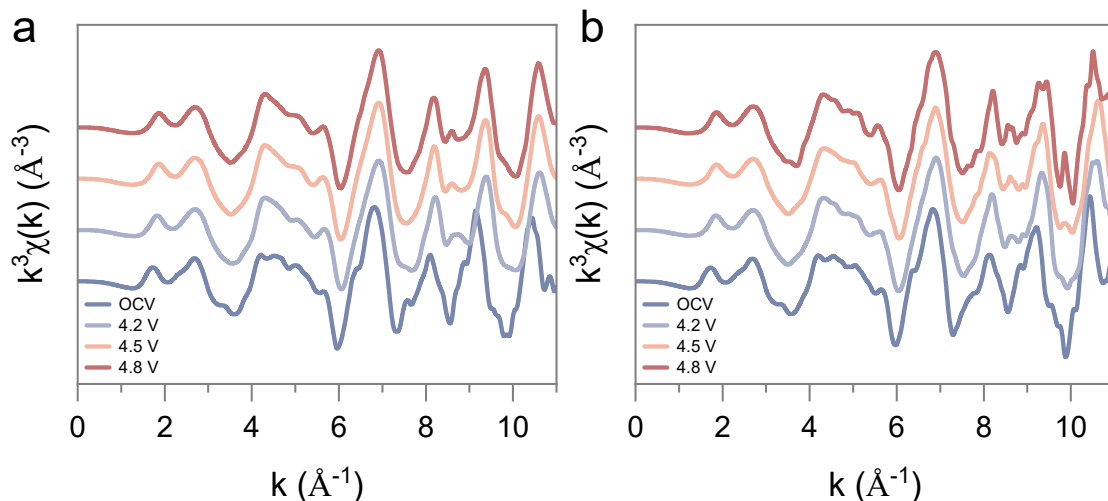


**Figure S4.  $k^3$ -weighted EXAFS oscillations at the Mn K-edge.** (a) Mn K-edge EXAFS spectra of  $\text{LiNi}_{1/3}\text{Co}_{1/3}\text{Mn}_{1/3}\text{O}_2$  (NCM333) at the pristine state and various charge states. (b) Mn K-edge EXAFS spectra of  $\text{LiNi}_{0.8}\text{Co}_{0.1}\text{Mn}_{0.1}\text{O}_2$  (NCM811) at the pristine state and various charge states. The distinct frequencies in  $\chi(k)$  correspond to different near-neighbor coordination shells. The smooth oscillation curves demonstrate high data quality, with the signal-to-noise ratio ensuring the credibility of subsequent analysis.

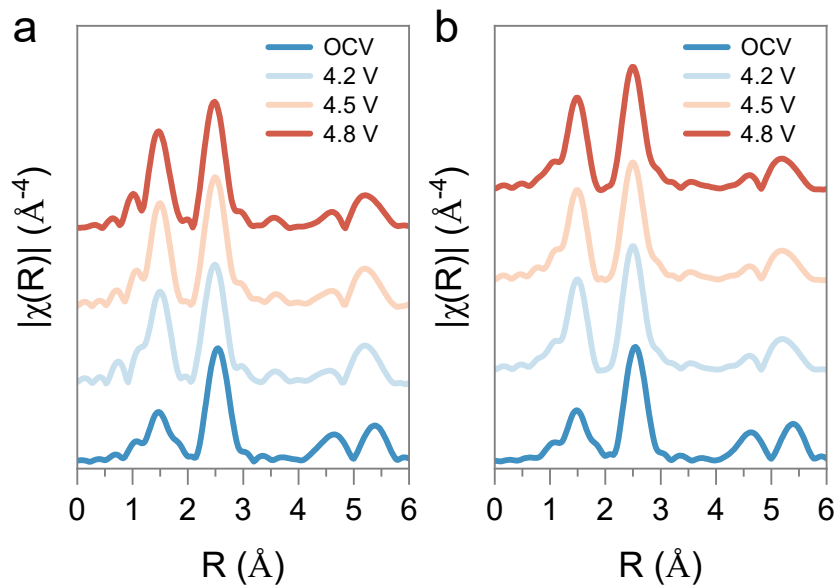


**Figure S5.  $k^3$ -weighted Fourier transform magnitudes of Ni K-edge EXAFS spectra.** (a) Fourier transform (FT) of Ni K-edge EXAFS spectra of  $\text{LiNi}_{1/3}\text{Co}_{1/3}\text{Mn}_{1/3}\text{O}_2$  (NCM333) at the pristine state and various charge states. (b) Fourier transform (FT) of Ni K-edge EXAFS spectra of  $\text{LiNi}_{0.8}\text{Co}_{0.1}\text{Mn}_{0.1}\text{O}_2$  (NCM811) at the pristine state and various charge states.

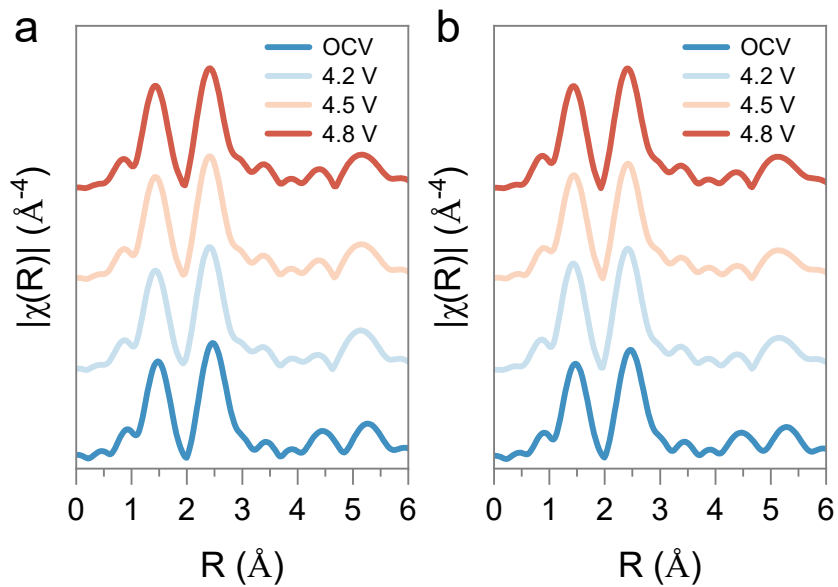


**Figure S6.  $k^3$ -weighted Fourier transform magnitudes of Co K-edge EXAFS spectra.** (a) Fourier transform (FT) of Co K-edge EXAFS spectra of  $\text{LiNi}_{1/3}\text{Co}_{1/3}\text{Mn}_{1/3}\text{O}_2$  (NCM333) at the pristine state and various charge states. (b) Fourier transform (FT) of Co K-edge EXAFS spectra of  $\text{LiNi}_{0.8}\text{Co}_{0.1}\text{Mn}_{0.1}\text{O}_2$  (NCM811) at the pristine state and various charge states.

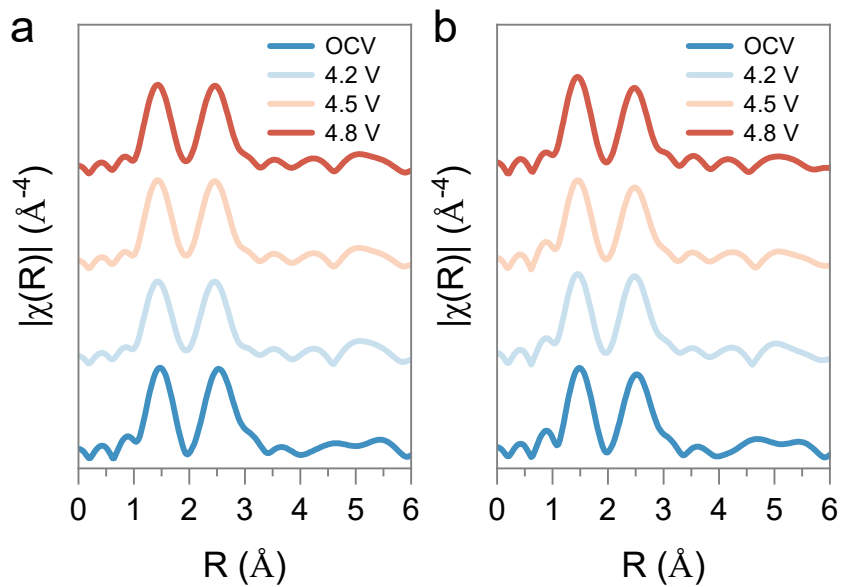


**Figure S7.  $k^3$ -weighted Fourier transform magnitudes of Mn K-edge EXAFS spectra.** (a) Fourier transform (FT) of Mn K-edge EXAFS spectra of  $\text{LiNi}_{1/3}\text{Co}_{1/3}\text{Mn}_{1/3}\text{O}_2$  (NCM333) at the pristine state and various charge states. (b) Fourier transform (FT) of Mn K-edge EXAFS spectra of  $\text{LiNi}_{0.8}\text{Co}_{0.1}\text{Mn}_{0.1}\text{O}_2$  (NCM811) at the pristine state and various charge states.

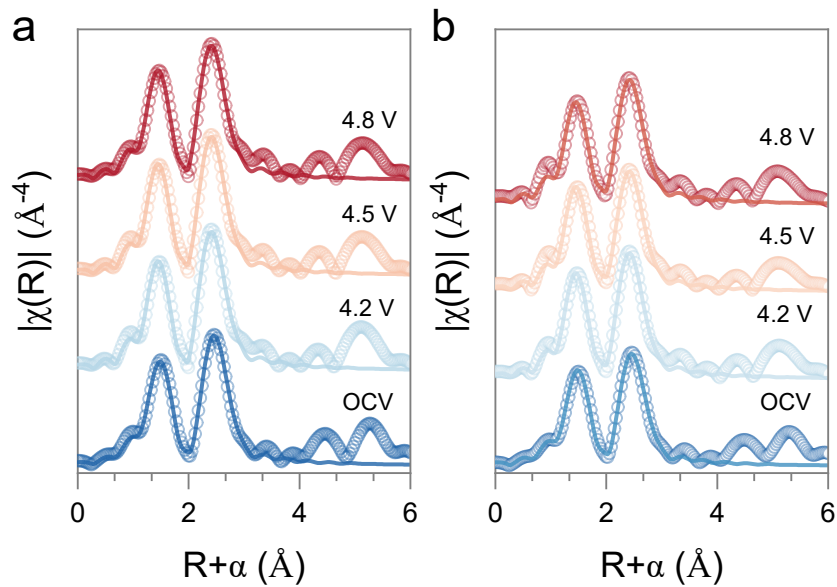


**Figure S8.  $k^3$ -weighted Fourier transform magnitudes with the best fitting results of Co K-edge EXAFS.** (a) Fourier transform (FT) of Co K-edge EXAFS spectra with the best fitting results of  $\text{LiNi}_{1/3}\text{Co}_{1/3}\text{Mn}_{1/3}\text{O}_2$  (NCM333) at the pristine state and various charge states. (b) Fourier transform (FT) of Co K-edge EXAFS spectra with the best fitting results of  $\text{LiNi}_{0.8}\text{Co}_{0.1}\text{Mn}_{0.1}\text{O}_2$  (NCM811) at the pristine state and various charge states.

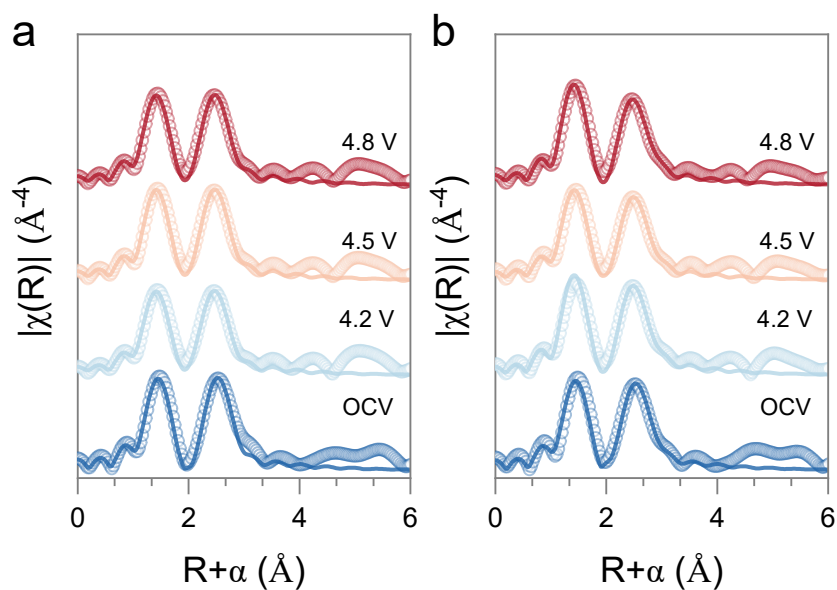


**Figure S9.  $k^3$ -weighted Fourier transform magnitudes with the best fitting results of Mn K-edge EXAFS.** (a) Fourier transform (FT) of Mn K-edge EXAFS spectra with the best fitting results of LiNi<sub>1/3</sub>Co<sub>1/3</sub>Mn<sub>1/3</sub>O<sub>2</sub> (NCM333) at the pristine state and various charge states. (b) Fourier transform (FT) of Mn K-edge EXAFS spectra with the best fitting results of LiNi<sub>0.8</sub>Co<sub>0.1</sub>Mn<sub>0.1</sub>O<sub>2</sub> (NCM811) at the pristine state and various charge states.

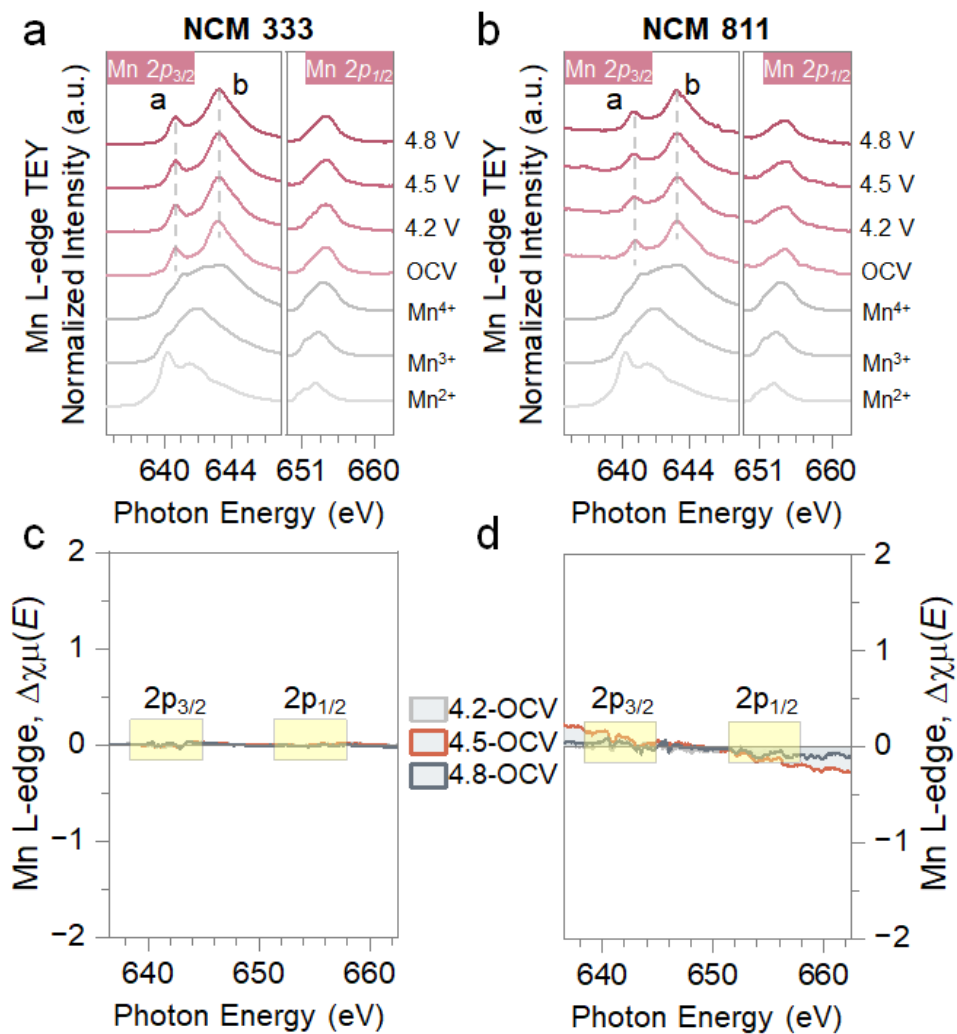


**Figure S10. Mn L<sub>2,3</sub>-edge spectra in TEY mode.** (a, b) Mn L<sub>2,3</sub>-edge NEXAFS of pristine and charged LiNi<sub>1/3</sub>Co<sub>1/3</sub>Mn<sub>1/3</sub>O<sub>2</sub> (NCM333) and LiNi<sub>0.8</sub>Co<sub>0.1</sub>Mn<sub>0.1</sub>O<sub>2</sub> (NCM811) to 4.2, 4.5, 4.8 V (vs. Li/Li<sup>+</sup>), respectively. (c, d) Differential spectra of Mn L<sub>2,3</sub>-edge of NCM333 and NCM811, respectively.

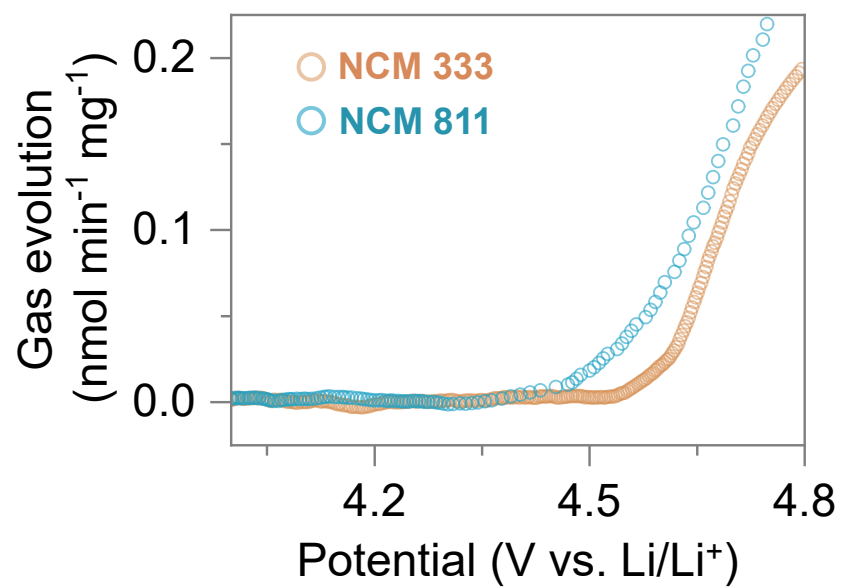


**Figure S11. Oxygen Release during Charging.** OEMS data was collected during the initial charge of NCM333 and NCM811 half-cells.

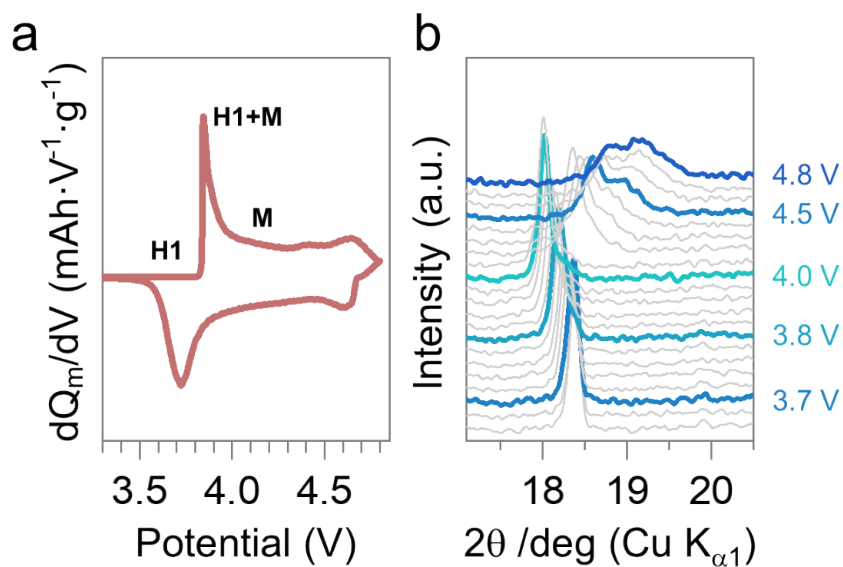


**Figure S12. Phase evolution of  $\text{LiNi}_{1/3}\text{Co}_{1/3}\text{Mn}_{1/3}\text{O}_2$  (NCM333).** (a) The  $dQ\cdot dV^{-1}$  profile of NCM333 was obtained from the charge-discharge curve. (b) Main peaks of the in-situ XRD pattern of NCM333 during charging to 4.8 V (vs Li/Li $^+$ ).

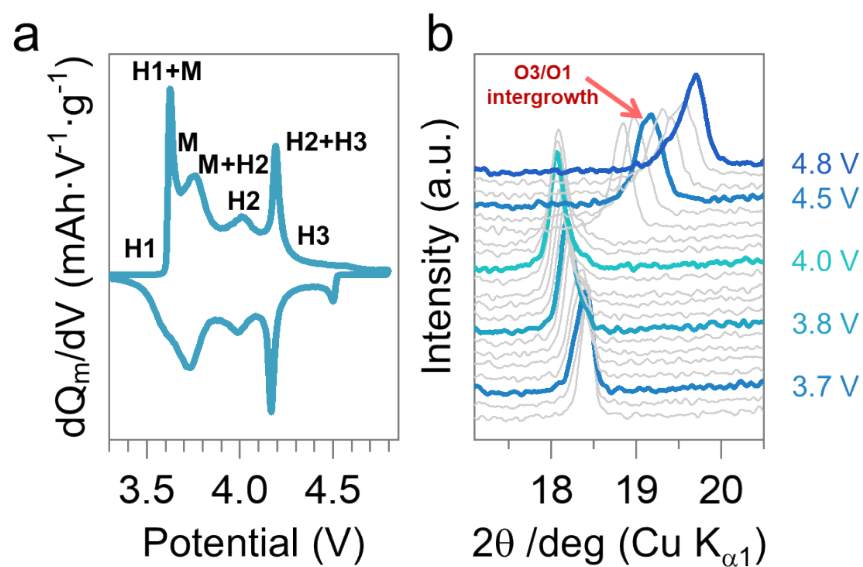


**Figure S13. Phase evolution of  $\text{LiNi}_{0.8}\text{Co}_{0.1}\text{Mn}_{0.1}\text{O}_2$  (NCM811).** (a) The  $dQ \cdot dV^{-1}$  profile of NCM811 was obtained from the charge-discharge curve. (b) Main peaks of the in-situ XRD pattern of NCM811 during charging to 4.8 V (vs Li/Li<sup>+</sup>).

**Tabel S1 The fitting parameters from Ni K-edge EXAFS spectra of NCM333**

Ni ( $S_0^2=0.85$ )	Scatting path	CN	$\sigma^2$ ( $\times 10^{-4}$ Å)	$\Delta E_0$ (eV)	$R_{\text{eff}}$ (Å)	R (Å)
Pristine (R factor = 0.0038)	Ni-O	5.9(7)	97(21)	2.1	1.96	1.96(1)
	Ni-TM	6.0(0)	47(3)	2.1	2.87	2.88(1)
4.2 V (R factor = 0.0075)	Ni-O	5.9(8)	39(40)	1.2	1.96	1.89(3)
	Ni-TM	6.0(0)	47(16)	1.2	2.87	2.82(2)
4.5 V (R factor = 0.0059)	Ni-O	6.1(4)	36(8)	1.2	1.96	1.89(1)
	Ni-TM	6.0(4)	42(3)	1.2	2.87	2.82(0)
4.8 V (R factor = 0.0079)	Ni-O	6.1(1)	41(21)	0.7	1.96	1.89(1)
	Ni-TM	6.0(0)	43(8)	0.7	2.87	2.82(1)

**Tabel S2 The fitting parameters from Co K-edge EXAFS spectra of NCM333**

Fe ( $S_0^2=0.80$ )	Scatting path	CN	$\sigma^2$ ( $\times 10^{-4}$ Å)	$\Delta E_0$ (eV)	$R_{\text{eff}}$ (Å)	R (Å)
Pristine (R factor = 0.0039)	Co-O	6	35(10)	-5.1	1.96	1.91(1)
	Co-TM	6	41(6)	-5.1	2.87	2.86(1)
4.2 V (R factor = 0.0089)	Co-O	6	38(9)	-6.3	1.96	1.89(1)
	Co-TM	6	42(6)	-6.3	2.87	2.81(1)
4.5 V (R factor = 0.0081)	Co-O	6	36(6)	-6.7	1.96	1.88(1)
	Co-TM	6	42(4)	-6.7	2.87	2.81(0)
4.8 V (R factor = 0.0074)	Co-O	6	36(14)	-6.9	1.96	1.88(1)
	Co-TM	6	43(10)	-6.9	2.87	2.81(1)

**Tabel S3 The fitting parameters from Mn K-edge EXAFS spectra of NCM333**

Mn ( $S_0^2=0.75$ )	Scatting path	CN	$\sigma^2$ ( $\times 10^{-4}$ Å)	$\Delta E_0$ (eV)	$R_{\text{eff}}$ (Å)	R (Å)
Pristine (R factor = 0.0237)	Mn-O	6	40(15)	2.7	1.96	1.90(2)
	Mn-TM	6	49(14)	2.7	2.87	2.90(2)
4.2 V (R factor = 0.0159)	Mn-O	6	47(14)	1.8	1.96	1.89(2)
	Mn-TM	6	59(13)	1.8	2.87	2.85(2)
4.5 V (R factor = 0.0146)	Mn-O	6	39(7)	1.6	1.96	1.89(1)
	Mn-TM	6	52(6)	1.6	2.87	2.85(1)
4.8 V (R factor = 0.0149)	Mn-O	6	40(22)	1.5	1.96	1.88(2)
	Mn-TM	6	52(20)	1.5	2.87	2.85(2)

**Tabel S4 The fitting parameters from Ni K-edge EXAFS spectra of NCM811**

Ni ( $S_0^2=0.85$ )	Scatting path	CN	$\sigma^2 (\times 10^{-4} \text{ \AA})$	$\Delta E_0$ (eV)	$R_{\text{eff}}$ (\AA)	R (\AA)
Pristine (R factor = 0.0027)	Ni-O	5.8(6)	94(17)	1.5	1.96	1.96(1)
	Ni-TM	6.0(0)	48(3)	1.5	2.87	2.88(0)
4.2 V (R factor = 0.0017)	Ni-O	5.7(3)	43(8)	1.0	1.96	1.89(0)
	Ni-TM	6.2(6)	49(7)	1.0	2.87	2.83(0)
4.5 V (R factor = 0.0019)	Ni-O	5.7(4)	44(6)	0.7	1.96	1.89(0)
	Ni-TM	6.0(4)	50(5)	0.7	2.87	2.83(0)
4.8 V (R factor = 0.0023)	Ni-O	5.7(4)	42(11)	0.9	1.96	1.89(1)
	Ni-TM	6.0(8)	48(9)	0.9	2.87	2.83(1)

**Tabel S5 The fitting parameters from Co K-edge EXAFS spectra of NCM811**

Fe ( $S_0^2=0.80$ )	Scatting path	CN	$\sigma^2 (\times 10^{-4} \text{ \AA})$	$\Delta E_0$ (eV)	$R_{\text{eff}}$ (\AA)	R (\AA)
Pristine (R factor = 0.0034)	Co-O	6	31(7)	-5.7	1.96	1.91(1)
	Co-TM	6	42(9)	-5.7	2.87	2.86(1)
4.2 V (R factor = 0.0063)	Co-O	6	26(7)	-6.3	1.96	1.88(1)
	Co-TM	6	37(5)	-6.3	2.87	2.82(1)
4.5 V (R factor = 0.0095)	Co-O	6	26(7)	-6.6	1.96	1.88(1)
	Co-TM	6	40(5)	-6.6	2.87	2.82(1)
4.8 V (R factor = 0.0082)	Co-O	6	29(8)	-6.3	1.96	1.88(1)
	Co-TM	6	37(6)	-6.3	2.87	2.82(1)

**Tabel S6 The fitting parameters from Mn K-edge EXAFS spectra of NCM811**

Mn ( $S_0^2=0.75$ )	Scatting path	CN	$\sigma^2 (\times 10^{-4} \text{ \AA})$	$\Delta E_0$ (eV)	$R_{\text{eff}}$ (\AA)	R (\AA)
Pristine (R factor = 0.0188)	Mn-O	6	44(13)	2.0	1.96	1.90(1)
	Mn-TM	6	54(11)	2.0	2.87	2.88(1)
4.2 V (R factor = 0.0096)	Mn-O	6	39(7)	0.9	1.96	1.88(1)
	Mn-TM	6	53(6)	0.9	2.87	2.83(1)
4.5 V (R factor = 0.0093)	Mn-O	6	42(10)	1.3	1.96	1.89(1)
	Mn-TM	6	59(9)	1.3	2.87	2.84(1)
4.8 V (R factor = 0.0092)	Mn-O	6	30(8)	0.9	1.96	1.88(1)
	Mn-TM	6	56(7)	0.9	2.87	2.83(1)

## References

1. B. Ravel and M. Newville, ATHENA, ARTEMIS, HEPHAESTUS: data analysis for X-ray absorption spectroscopy using IFEFFIT, *J. Synchrotron Radiat.*, 2005, **12**, 537-541.
2. J. Rehr, R. Albers and S. Zabinsky, High-order multiple-scattering calculations of X-ray-absorption fine structure, *Phys. Rev. Lett.*, 1992, **69**, 3397.
3. P. A. O'Day, J. J. Rehr, S. I. Zabinsky and G. E. Brown, Jr., Extended X-ray Absorption Fine Structure (EXAFS) Analysis of Disorder and Multiple-Scattering in Complex Crystalline Solids, *J. Am. Chem. Soc.*, 1994, **116**, 2938-2949.
4. E. Stavitski and F. M. De Groot, The CTM4XAS program for EELS and XAS spectral shape analysis of transition metal L edges, *Micron*, 2010, **41**, 687-694.
5. C. Schulz, K. Lieutenant, J. Xiao, T. Hofmann, D. Wong and K. Habicht, Characterization of the soft X-ray spectrometer PEAXIS at BESSY II, *J. Synchrotron Radiat.*, 2020, **27**, 238-249.
6. K. Momma and F. Izumi, VESTA 3 for three-dimensional visualization of crystal, volumetric and morphology data, *J. Appl. Crystallogr.*, 2011, **44**, 1272-1276.
7. H. Dau, P. Liebisch and M. Haumann, X-ray absorption spectroscopy to analyze nuclear geometry and electronic structure of biological metal centers--potential and questions examined with special focus on the tetra-nuclear manganese complex of oxygenic photosynthesis, *Anal Bioanal Chem*, 2003, **376**, 562-583.